Numerical Investigation of Laminar to Turbulent Boundary Layer Transition on a Naca 0012 Airfoil for Vertical-Axis Wind Turbine Applications

Marco Raciti Castelli*, Francesco Garbo, Ernesto Benini**
Department of Mechanical Engineering – University of Padova
Via Venezia, 1 – 35131 Padova, Italy
E-mail address: *marco.raciticastelli@unipd.it, **ernesto.benini@unipd.it

ABSTRACT

Laminar to turbulent transition in vertical-axis wind turbines has a dramatic effect on overall rotor performance, especially in fast rotating machines, where reliable prediction of the total drag coefficient for high values of tip speed ratio is one of the most critical topic in CFD simulations.

This paper presents a 2D numerical investigation of the capability of the γ–θ transition model to predict the laminar to turbulent transition and consequent friction drag over a NACA 0012 airfoil for a Reynolds number of 360,000, which is typical of vertical-axis wind turbine blades during operation. The analized range of angles of attack varies from 0 deg to 10 deg. The commercial CFD solver ANSYS FLUENT® is used.

In particular, the sensitivity to grid resolution is investigated for four different architectures: a completely unstructured mesh, a hybrid structured-triangular one and two distinct hybrid structured-triangular meshes where the wake region behind the airfoil is discretized using a fully structured grid. The effect of freestream turbulence intensity on the transition onset is also analyzed.

Finally, CFD results are compared to experimental data, although affected by some uncertainty, and to the predictions of an interactive program for the design and analysis of subsonic isolated airfoils (XFOIL), showing a very good agreement provided that the value of freestream turbulence intensity is known.

NOMENCLATURE

c [mm]   blade chord
C_D [-]   airfoil total drag coefficient
$C_{D,pressure}$ [-]   airfoil total pressure drag coefficient
$C_{D,skin}$ [-]   airfoil total skin friction drag coefficient
c_f [-]   airfoil local skin friction coefficient
C_L [-]   airfoil total lift coefficient
D [N]   airfoil total drag
$D_{pressure}$ [N]   airfoil total drag due to pressure distribution
D_{skin} [N]   airfoil total drag due to skin friction distribution
$FSTI$ [%]   percent freestream turbulence intensity
K [m²/s²]   turbulent kinetic energy

L [N]   airfoil lift

R [mm]   wind turbine radius

Re [–]   Reynolds number relative to airfoil

Re_θ [–]   momentum thickness Reynolds number

TSR [–]   tip speed ratio

V [m/s]   wind velocity at rotor disk

V_∞ [m/s]   unperturbed wind velocity at computational domain entrance

y [m]   distance between wall and relative grid cell centroid

y^+ [–]   dimensionless distance between wall and relative grid cell centroid

A.O.A. [deg]   airfoil angle of attack

θ [m]   momentum thickness

μ [Pa·s]   air viscosity

v [m²/s]   air kinematic viscosity

μ [kg/(m·s)]   air viscosity at average room temperature

μ_τ [m/s]   friction velocity

ρ [kg/m³]   air density

τ_w [N/m²]   wall shear stress

ω [rad/s]   wind turbine angular velocity

1. INTRODUCTION AND BACKGROUND

Laminar to turbulent transition in low Reynolds wall boundary layers is of significant importance in modern subsonic aerodynamics for the design of vertical-axis wind turbines.

A growing interest is being registered in recent years for MW scale VAWTs, especially for offshore applications [1] and international partners from the wind industry and research community will further explore the idea of high size floating VAWTs [2] [3]. Nevertheless, the largest amount of VAWT market is today represented by small scale rotors (up to 6 kW nominal power), which are seen as potentially playing an important part in the future electricity generation mix. [4]. As Reynolds number is proportional to freestream velocity and airfoil chord, the relative low range of operating velocities and the small typical chord values of small wind turbine blades correspond to low Reynolds numbers. As pointed out by Chawla [5], at low Reynolds number airfoils generate lower lift and encounter higher drags, determining a general decay in overall blade performance. For low Reynolds number flows, blade boundary layer often remains laminar in the adverse pressure gradient region, with consequent flow separation and formation of eddies, resulting in an increased airfoil drag. As reported by Koch [6] and Mueller [7], due to the unpredictibility of the the effects of laminar separation and reattachment, full knowledge of low Reynolds boundary layer behaviour and of blade skin friction distribution is still a challenging task, both experimentally and numerically. In particular, vertical axis wind turbines show an inherently non-stationary aerodynamic behaviour, mainly due to the continuous variation of the blade angle of attack during the rotation of the machine: this peculiarity involves the continuous variation both of the relative velocity with respect to the blade profile and - although to a lesser extent - of the corresponding Reynolds number [8]. This phenomenon, typical of slow rotating machines, has a significant effect both on the dynamic loads acting on the rotor and on the generated power and, therefore, on performance.

Classical aerodynamic tools, such as the theory of blade elements (BE-M) [9] [10], while presenting the certain advantage of low computation efforts, are nevertheless limited by the availability of airfoil databases. Since most databases available in literature are derived from aeronautical applications, referring to relatively high Reynolds numbers

(above Re = 1,000,000) [11], it has been recognized that there is a paucity of accurate airfoil data needed to describe the aerodynamics of wind turbine blades. This limits vertical axis wind turbine classical analysis to a narrow number of blade profiles, substantially some NACA series symmetrical airfoils, for which low Reynolds number extended databases are available in literature [12].

The use of a panel method, such as in XFOIL [13] [14] [15], could be a really powerful design tool for predicting turbulent transition and consequent friction drag, but is limited to attached flows, thus frustrating the chance to derive an extended airfoil database (to be used in BE-M codes) simply by numerical calculations.

The limitations in low Reynolds number accurate aerodynamic databases can be overcome by the use of CFD codes, which can outflank the lack of airfoil data thanks to their inherent ability to determine the aerodynamic components of actions through the integration of the Navier-Stokes equations in the neighborhood of the wind turbine blade profile [16]. Raciti Castelli et al. [17] performed a full CFD campaign of simulations of the behaviour of a straight-bladed VAWT made of three NACA 0021 airfoils of 85.8 mm chord. The work evidenced a gradual decrease in airfoil relative angle of attack passing from lower to higher TSR values, defined as:

$$TSR = \omega R \, / \, V_\infty \tag{1}$$

As a matter of fact, in the latter case, computed angles of attack are relatively small, being determined to a greater extent by blade relative velocity and to a lesser extent by wind velocity at rotor disk section, as can be seen in Figure 1, showing a comparison between blade relative angle of attack for low and high TSR operating conditions.

Two distinct rotor blade operating conditions can be identified:

· moderate to deep stall for rotor operation from lower to optimal TSR values;
· below stall for rotor operation at higher TSR values.

Classical turbulence models, although widely used to calculate the pressure loads acting on blade profiles, are unable to predict the laminar-turbulent transition, resulting in poor prediction of rotor performance, caused by the overestimation of airfoil friction drag due to a fully turbulent-regime flow computation [18], expecially for high values of tip speed ratio where, due to the low range of blade relative angles of attack, the skin friction contribution to overall airfoil drag is quite relevant.

Lombardi et al. [19] tested the capability of a classical RANS solver in predicting the friction drag over a NACA 0012 airfoil for 0 deg angle of attack and compared CFD results with the values given by a coupled potential/boundary-layer method. The analized range of Reynolds numbers varied from 300,000 to 9,000,000. As can be seen in Figure 2, being the local skin friction coefficient defined as:

$$c_f = \frac{\tau_w}{\frac{1}{2}\rho c V_\infty^2} \tag{2}$$

the relative integral over the whole airfoil lenght resulted overestimated by all turbulence models - even using highly refined grids - because of their inherent inability to predict the boundary layer transition.

Lian and Shyy [20] coupled a Navier-Stokes solver (featuring e^N transition model) and a Reynolds-averaged two-equation closure to study laminar to turbulent low Reynolds number
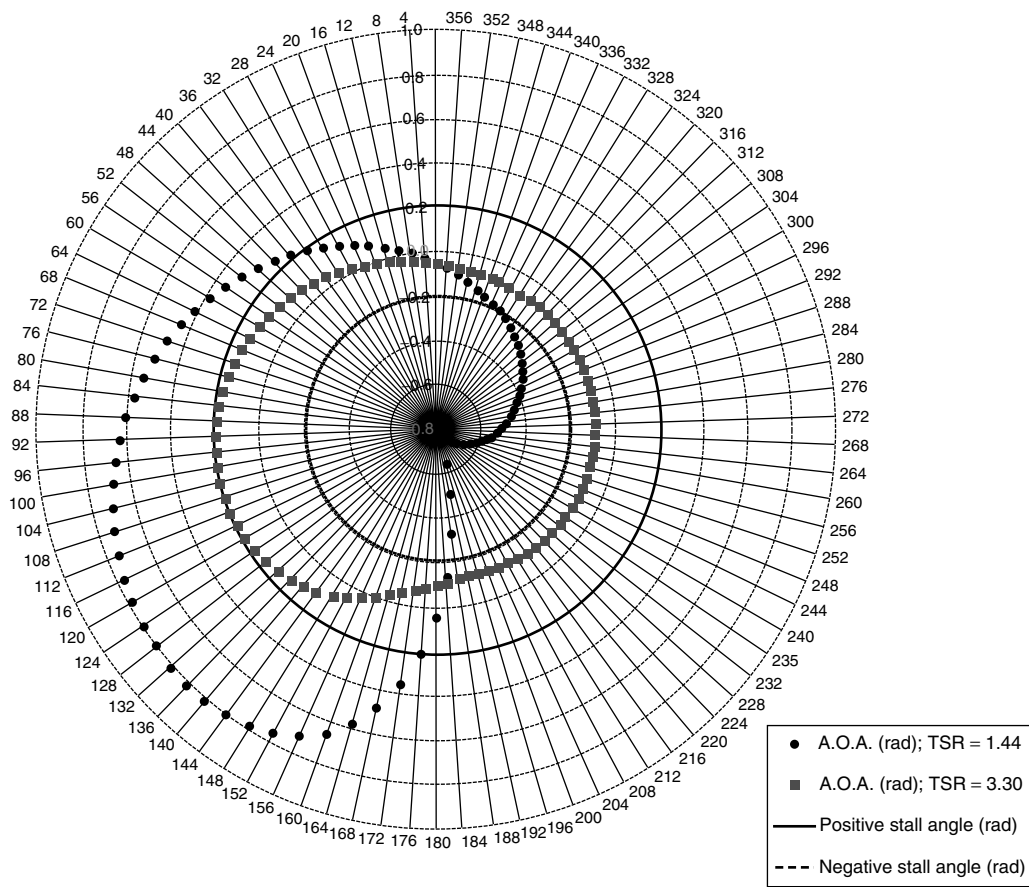
Figure 1: Gradual decrease in airfoil relative angle of attack passing from lower (circle) to higher (squre) TSR operating values for a straight-bladed Darrieus made of three NACA 0021 airfoils (from: [17]).
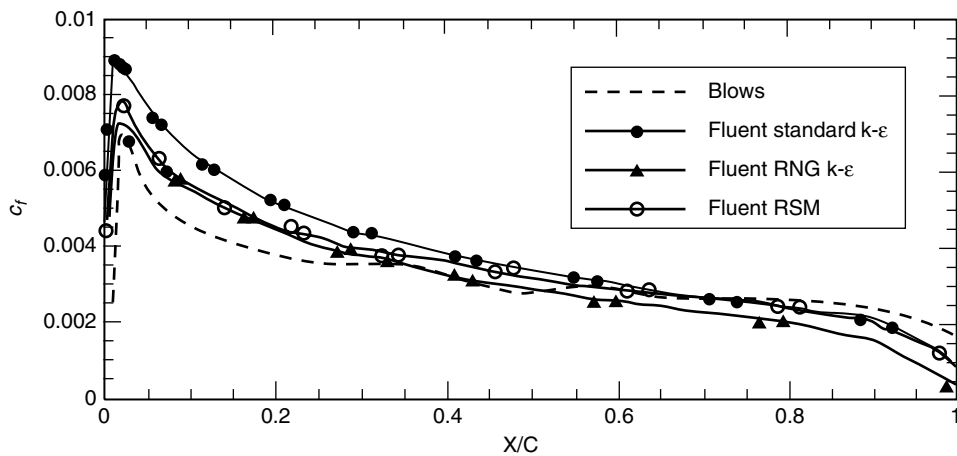

Figure 2: Skin friction drag comparison between a coupled potential/boundary layer method (Blows) and three classical turbulence models for Re = 300,000 (from [19]). As can be noticed, no transition is predicted.

flows, characterized by laminar separation and transition, around a SD7003 airfoil, obtaining good agreement between numerical prediction and experimental measurements regarding the transition location as well as overall flow structures. It was also noticed that the transition

onset is affected by a large spectrum of disturbances, such as freestream turbulence, wall roughness, pressure gradient, acoustic noise, wall suction or blowing and wall heating or cooling, concluding that a comprehensive transition model considering all these factors is not yet available.

γ–θ model developed by Menter et al. [21], [22] is one of the first transition prediction tools available in a commercial flow solver, which is compatible with modern CFD approaches, such as unstructured grids and massive parallel executions. The model is based on two transport equations, one for intermittency and one for the transition onset criteria in terms of momentum thickness Reynolds number, defined as:

$$\mathrm{Re}_{\theta} = \frac{V_{\infty}\theta}{\upsilon} \qquad (3)$$

The proposed transport equations do not attempt to model the physics of the transition process but form a framework for the implementation of correlation-based models into general-purpose CFD methods. A significant number of test cases have been used to validate the transition model for turbomachinery and aerodynamic applications, including a 2D horizontal-axis wind turbine airfoil section [22]. In this case, transition has been predicted to occur slightly too far upstream for all angles of attack. One possible explanation for this behaviour is that the transition model was developed mainly for internal turbomachinery, thus paying little attention to turbulence lenght-scale effects, which are likely to play an important role in predicting transition for low-speed external flows, such as wind turbine airfoils.

Benini and Ponza [23] investigated the capability of the γ–θ transition model in predicting the laminar to turbulent transition in the boundary layer developing around a supercritical airfoil (NLR 7301). The explored range of Mach numbers varied from 0.3 to 0.825, thus covering a fully transonic regime. The maximum discrepancy between the predicted and experimental lift coefficient resulted in the order of +5%, while the drag coefficient evidenced a maximum discrepancy of +21%. The numerical results showed a certain degree of sensitivity to the turbulence intensity level set at the domain inlet, being the transition onset moved foreward with increasing turbulence levels.

Hosseinverdi and Boroomand [24] tested the capability of two empirical correlations (Cebeci & Smith and e^{N} method) coupled to the two-equation SST k–ω turbulence model of Menter, in order to predict the incompressible transitional flow over a S809 wind turbine airfoil, obtaining significant improvements in drag prediction by using the transitional computation in comparison with the fully turbulent simulation.

Wang et al. [25] investigated numerically the dynamic stall occurring to a NACA 0012 oscillating airfoil pitching in a sinusoidal pattern in the low Reynolds number fluid flow regime. A comparison with experimental data proved the SST k-ω based DES approach to be superior with respect to the γ–θ transition model for very high angles of attack, where massive flow separations are encountered, especially for the downstroke phase of oscillation.

The main objective of the present study is to propose a new VAWT performance prediction strategy based on the diversification of the numerical approach between lower and higher TSR operating ranges, in order to enhance the capability of the (from time to time) selected turbulence model to precisely reproduce the main characteristic flow structures. While the candidate turbulence model for rotor operation from lower to optimal TSR values should be able to reproduce flow separation and adverse pressure gradients, advance in high TSR values operation prediction capability depends on the attitude of the turbulence model to

determine laminar to turbulent transition, in order not to underestimate rotor performance because of the overshooting of blade friction drag. For this purpose, the present work performs a 2D numerical investigation of the capability of the γ–θ transition model to predict the laminar to turbulent transition and consequent friction drag over a 85.8 mm chord NACA 0012 airfoil for a low Reynolds number (360,000), which is typical of vertical-axis wind turbine blades during operation, limiting the focus of the research on the effect of grid architecture and freestream turbulence. As a first phase of an extensive analysis of a VAWT operation, the high TSR rotating airfoil range is investigated by exploring the range of angles of attack from 0 to 10 deg, thus remaining just below the stall limit.

The sensitivity to grid resolution is investigated for four different mesh architectures at 0 deg angle of attack:

- a completely unstructured mesh, named *Model 0*;
- a hybrid structured-triangular mesh, named *Model 1*;
- a hybrid structured-triangular mesh where the wake region behind the airfoil is discretized using a horizontal fully structured grid, named *Model 2*;
- a hybrid structured-triangular mesh where the wake region behind the airfoil is discretized using a diverging fully structured grid in order to better capture wake region flow structures, named *Model 3*.

The effect of freestream turbulence intensity on the transition onset and consequent airfoil skin friction coefficient distribution is also analyzed.

CFD results are compared to experimental data from Sheldal and Klimas [12], who performed low to moderate Reynolds number wind tunnel tests for some blade candidate airfoil sections (among which, NACA 0012) in order to properly describe the aerodynamics of wind turbine blades.

In order to overcome the lack of experimental data on skin friction drag distribution, CFD results are compared to the predictions of an interactive program for the design and analysis of subsonic isolated airfoils (XFOIL), showing a very good agreement provided that the value of freestream turbulence intensity is known.

2. THE CASE STUDY

In order to check the capabilities of the γ–θ transitional model, a selection of experimental data from Sheldahl and Klimas [12] was assumed as a test case: a NACA 0012 blade profile made of aluminium was tested in the Walter H. Beech Memorial Low-Speed Wind Tunnel at Whichita State University. The tunnel was made of a 2.13×3.05 m test section fitted with floor to ceiling two-dimensional inserts, in order to reduce three-dimensional effects. The tested airfoil section presented a 15.24 cm chord and a 0.91 m span. The explored Reynolds number was 360,000.

The positive full range section total lift and drag coefficients, defined as:

$$C_L = \frac{L}{\frac{1}{2}\rho c V_\infty^2} \qquad (4)$$

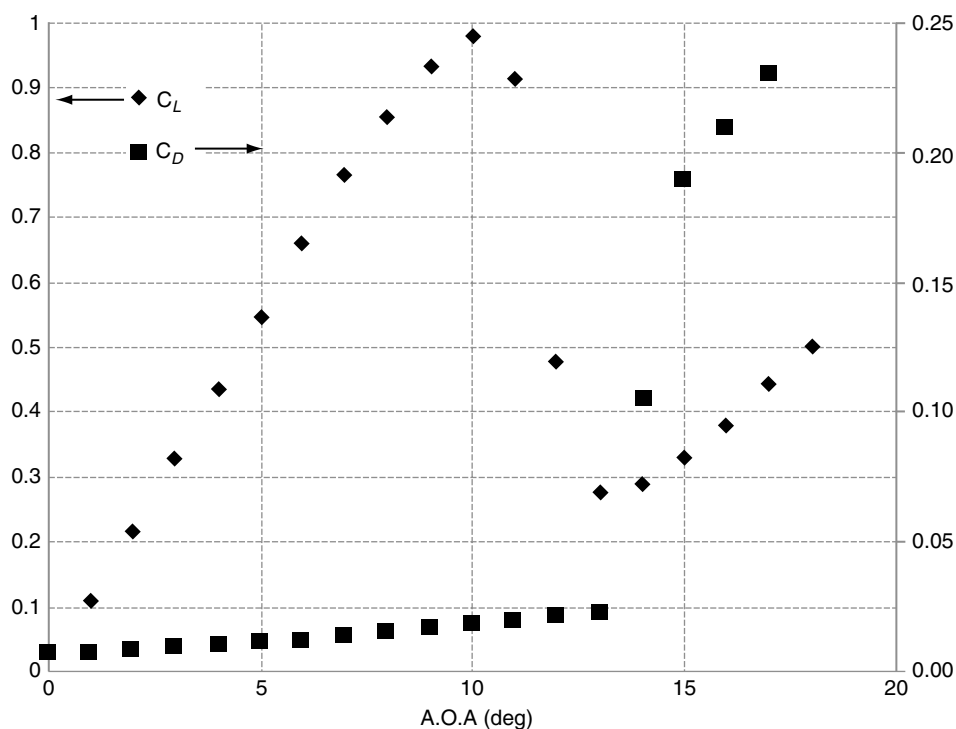$$C_D = \frac{D}{\frac{1}{2}\rho c V_\infty^2} \qquad (5)$$

are shown in Figure 3.

Figure 3: Section lift and drag coefficients for NACA 0012 airfoil at Re = 360,000 (from [12]).

The explored range of angles of attack varied from 0 deg to 180 deg. Anyway, it was noticed that, for angles of attack greater than 25 deg, aerodynamic coefficient of different airfoil sections became very similar, being the total drag force due more to wake drag than to skin friction drag. In fact, as pointed out by Sheldahl and Klimas [12] the effect of the Reynolds number (in the range of 350,000 to 700,000) and the airfoil geometry have little effect on the lift coefficient in the angle of attack range of 25 to 180 deg.

For this reason, being interested to the effect of laminar to turbulent transition on the skin friction coefficient distribution, CFD investigations were limited to a quite small range [0 deg – 10 deg] of angles of attack.

Unfortunately, the turbulence intensity was not clearly defined: practical considerations about the type of wind tunnel used in the experiments [26] suggested that low turbulence intensity were to be expected. Therefore, different values of percent free-stream turbulence intensity values, defined from the following relation:

$$FSTI = \frac{100}{V_\infty} \cdot \sqrt{\frac{2}{3}K}$$

(6)

ranging from 1 to 1.5% were investigated.

3. MODEL GEOMETRY AND COMPUTATIONAL GRIDS

All the grids adopted for the present work had common geometric features, except for the areas close to the airfoil and (for *Model 2* and *Model 3*) the wake region. As the aim of the numerical simulations was to explore the 2D flow field close to a blade profile, the computational domain was discretized into two macro-areas:

· a rectangular outer zone, identified as *Wind Tunnel sub-grid*, determining the overall computational domain, with a circular (for *Model 0* and *Model 1*) or

complex-geometry (for *Model 2* and *Model 3*) opening centered on airfoil centre of pressure, which for a NACA 0012 profile is located at 25% of chord length;

· a circular (for *Model 0* and *Model 1*) or complex-geometry (for *Model 2* and *Model 3*) inner zone, which was identified as *Airfoil sub-grid*, were grid points were clustered in order to obtain an accurate mesh setup of wall boundary layer and also of airfoil wake.

3.1. Wind tunnel sub-grid

Figures 4 through 6 show the main dimensions and the boundary conditions of the *Wind Tunnel sub-grid* area for each mesh configuration.

The computational domain width was set to 20 blade chords, so as to reproduce both the solid and wake blockage effects of the experimental measurements [26]. In order to allow a full development of the wake behind the airfoil, inlet and outlet boundary conditions were placed respectively 10 blade chord upwind and 30 blade chord downwind with respect to airfoil test section.

Two *symmetry* boundary conditions were used for the two side walls. The boundary between *Wind Tunnel sub-grid* and *Airfoil sub-grid* was set as an *interior*, thus ensuring the continuity of the flow field.

A totally unstructured mesh was chosen for the *Wind Tunnel sub-grid*, in order to reduce engineering time to prepare the CFD simulations. Figures 7 through 9 display *Model 1*, *Model 2* and *Model 3* meshes, while Table 1 shows the main characteristics of the four grid architectures.

3.2. Airfoil sub-grid

Being the area close to the airfoil section, great attention was directed to the *Airfoil sub-grid*. The most important differences between the various meshes adopted in the present work were concentrated in this area. The option of further dividing the computational domain into
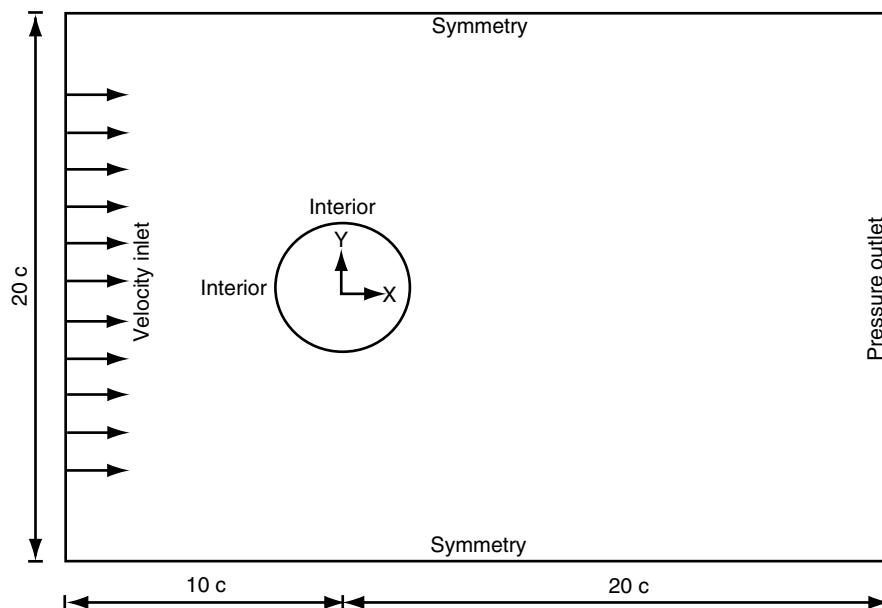

Figure 4: Main dimensions and boundary conditions of the *Wind Tunnel sub-grid* area for *Model 0* and *Model 1*.
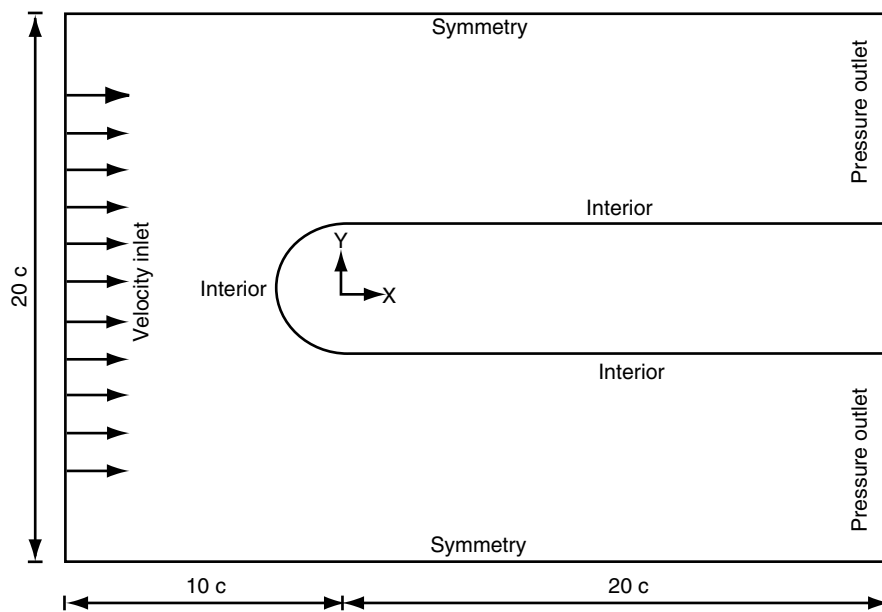
Figure 5: Main dimensions and boundary conditions of the *Wind Tunnel sub-grid* area for *Model 2.*
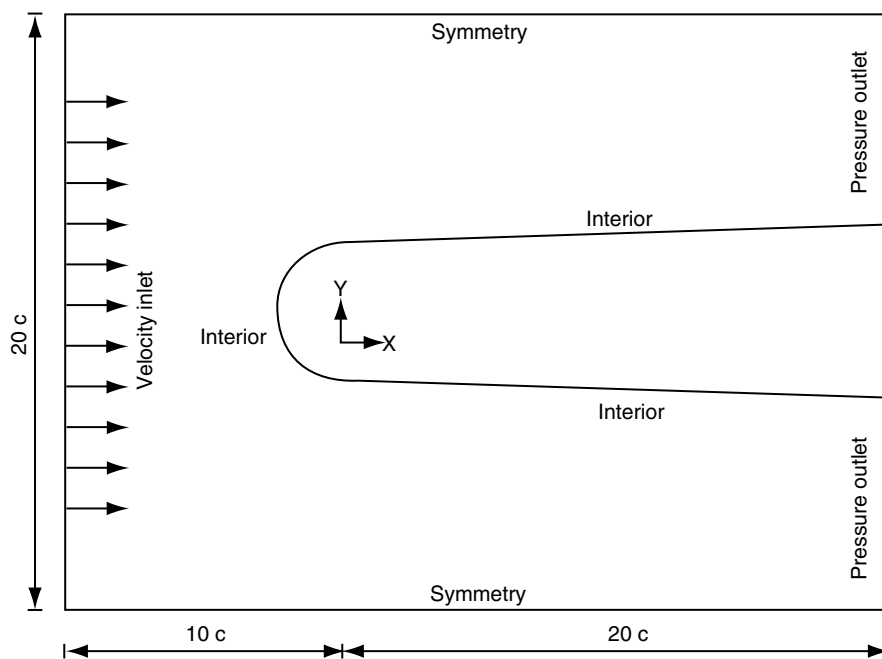

Figure 6: Main dimensions and boundary conditions of the *Wind Tunnel sub-grid* area for *Model 3.*

a small sub-grid makes it possible to use a highly refined grid close to blade profiles without requiring a large mesh with over-refinement in areas of lower importance.

The computational grids around blade profiles were constructed from lower topologies to higher ones, adopting appropriate size functions, in order to cluster grid points near the leading edge and the trailing edge of the blade profile, so as to improve the CFD code capability of determining lift, drag and the laminar to turbulent transition onset.

A high-quality mesh was created close to the airfoil surface with the purpose of better capturing the surface boundary layer and to obtain y^+ values close to 1. This parameter is a
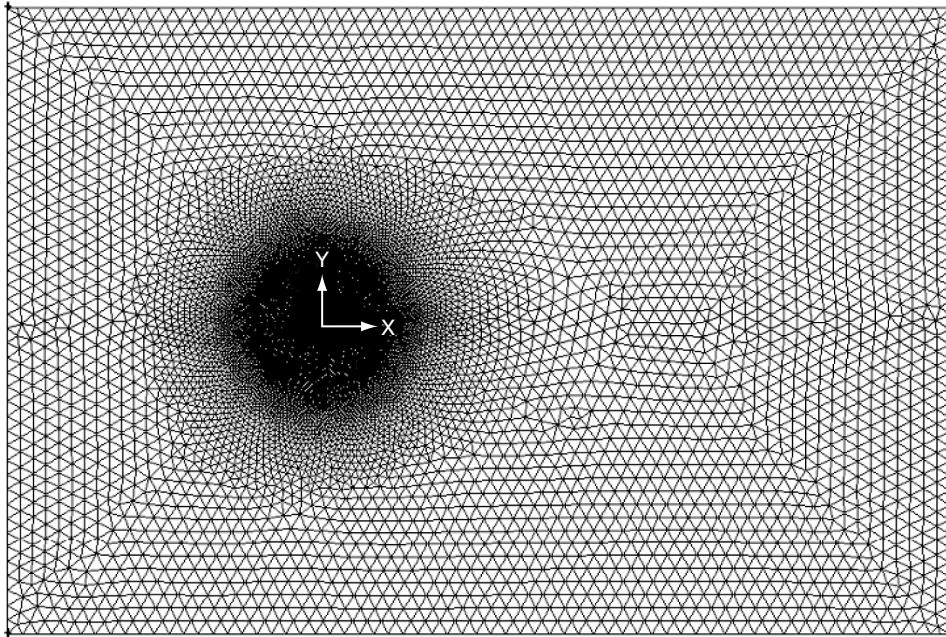
Figure 7: *Model 1* mesh.
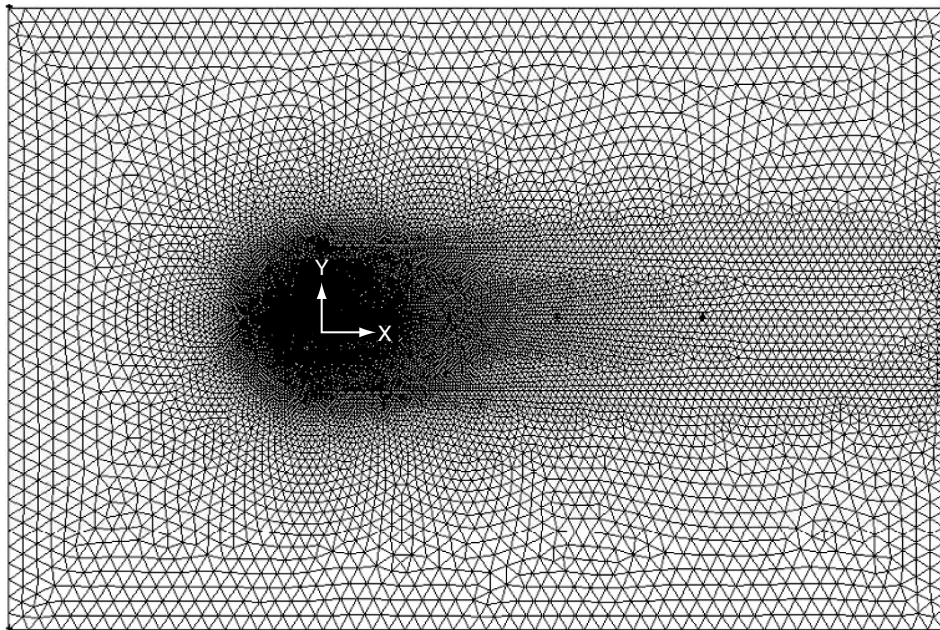
Figure 8: *Model 2* mesh.

mesh-dependent dimensionless distance that quantifies the degree of wall layer resolution, in formulas:

$$y^+ = \rho\,\mu_\tau\,y/\mu \qquad\qquad (7)$$

It is worth remembering that, if the y^+ parameter violates the constraints imposed by the choice of the turbulence model, the wall shear stress is not satisfactory calculated, thus leading to fairly incorrect results.
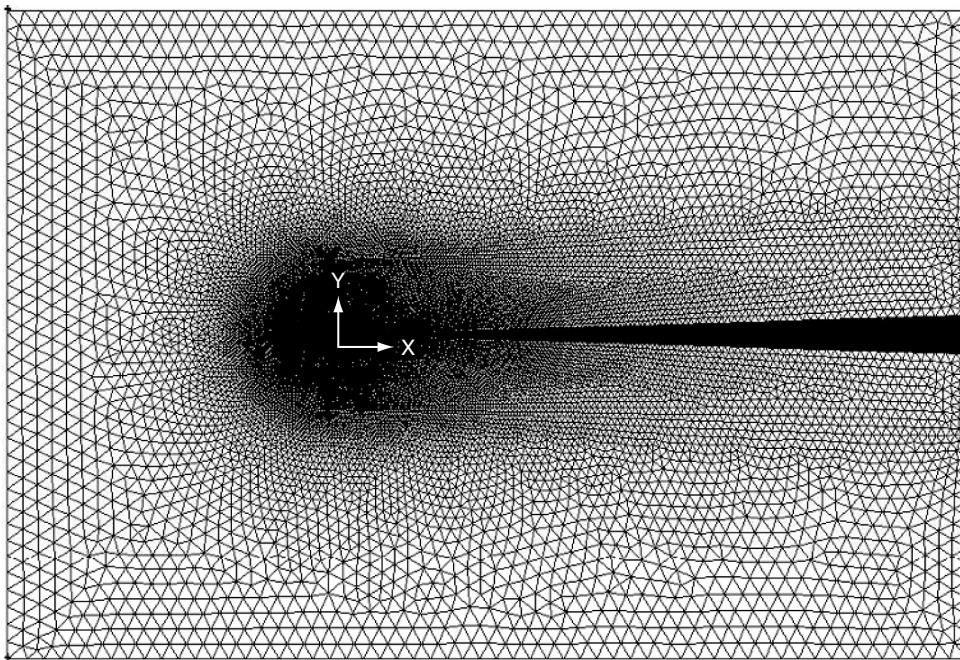
Figure 9: *Model 3* mesh.

Table 1: *Wind tunnel sub-grid* main characteristics

Grid points minimum spacing on *Interior* boundary condition [mm]	4
Growth factor from airfoil Distribution of grid points on airfoil [–]	1.1
Grid points maximum spacing on external boundary conditions [mm]	40 (*Model 0*, *Model 1*) 45 (*Model 2*, *Model 3*)

The main characteristics of the four examined *Airfoil sub-grid* architectures will be described in the following sections.

3.3. *Model 0* airfoil sub-grid

An isotropic unstructured mesh was chosen for *Model 0 Airfoil sub-grid*, in order to test the model prediction capability on a very simple grid. Considering their features of flexibility and adaption, unstructured meshes are in fact very easy to obtain, also for complex geometries, and often represent the "first attempt" in order to get a quick response from CFD in engineering work.

The airfoil was enclosed inside a control circle of 2.4 chord diameter, centered on airfoil centre of pressure. This geometry, which was set as an *interior* boundary condition, has no physical significance: its aim was to allow a precise dimensional control of the grid elements in the area close to the airfoil by adopting a first size function operating from the blade profile to the control circle itself and a second size function operating from the control circle to the whole *Wind Tunnel sub-grid* area, as described before.

Figure 10 shows the main dimensions and the boundary conditions of *Model 0 Airfoil sub-grid* area, while Table 2 reports the characteristic data of grid boundary layers. Two meshes have been prepared in order to test the code sensitivity to grid resolution.
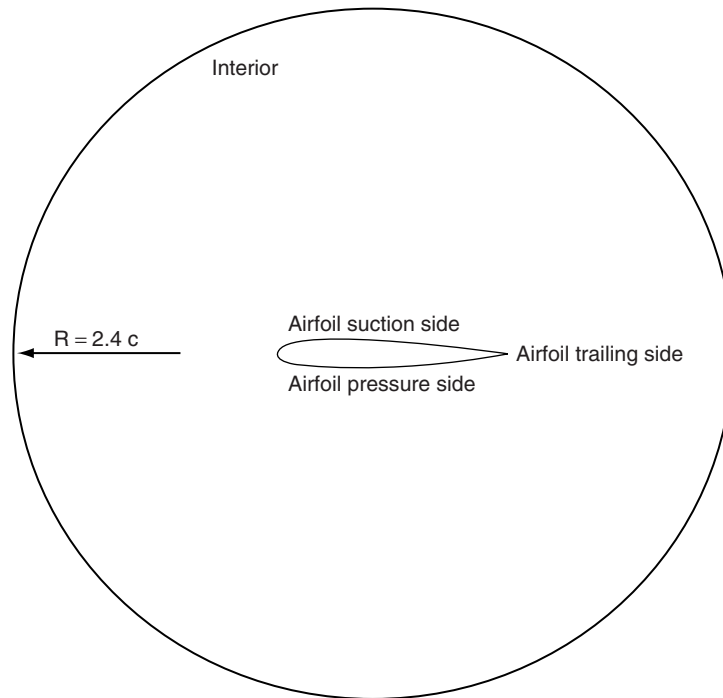
Figure 10: Main dimensions and boundary conditions of the *Airfoil sub-grid* area for *Model 0.*

Table 2: Characteristic data of grid boundary layers for *model 0* meshes

Mesh name	1.10	1.05
Number of grid points on airfoil		
upper/lower surface [–]	3500	4000
Distribution of grid points on airfoil	double sided	double sided
	successive ratio 1.0001	successive ratio 1.0000
Growth factor from airfoil [–]	1.10	1.05

In Figure 11 (a) a view of the global mesh is depicted, while Figures 11 (b), (c) show some details of the grid boundary layer around the airfoil close to the leading edge and the trailing edge regions respectively.

3.4. *Model 1* airfoil sub-grid

Also for *Model 1 Airfoil sub-grid* the profile was enclosed in a control circle of 2.4 chord diameter, centered on airfoil centre of pressure. A high-quality structured mesh was created close to the airfoil surface in order to better capture the boundary layer, while outside the boundary layer region a triangular unstructured grid was created using proper size functions.

In Figure 12 (a) a view of the global mesh is depicted, while Figures 12 (b), (c) show some details of the grid boundary layer around the airfoil close to the leading edge and the trailing edge regions respectively.

Mesh names were characterized by three cifres, representing respectively the number of grid points on airfoil upper/lower surface, the thickness [mm] of the boundary layer first row and the growth factor from the airfoil surface. In order to test the code sensitivity to grid resolution, some different grid parameters were modified:

- the height of the first cell row, which directly influences the value of y^+ (from *Model 1 - 350 006 1.025* to *Model 1 - 350 010 1.500*);
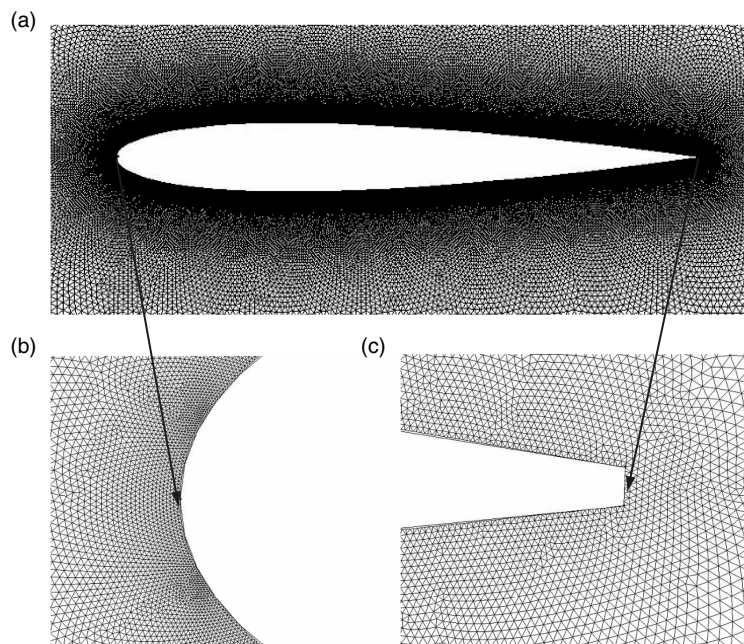
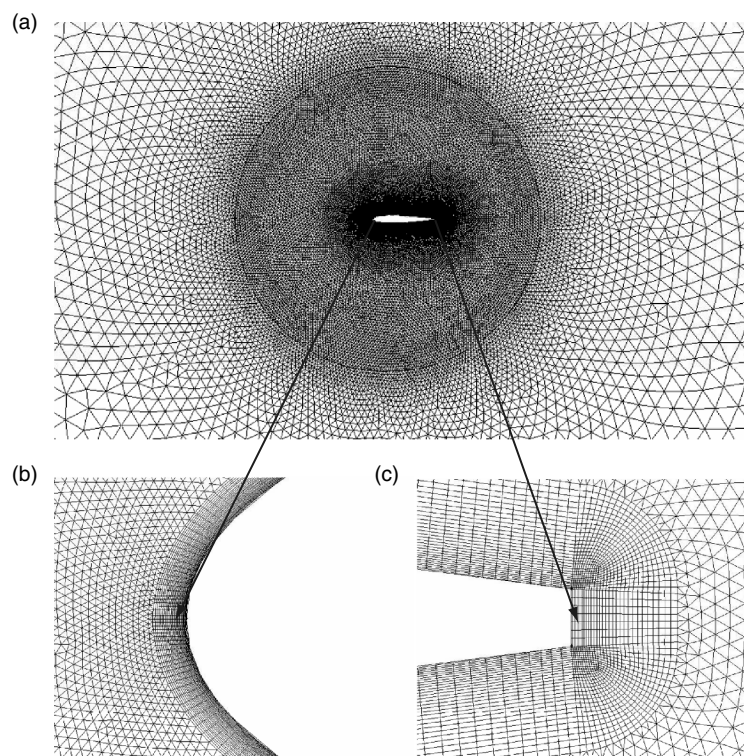Figure 11: *Model 0* – 1.05 *Airfoil sub-grid* mesh.

Figure 12: *Model 1* – 006 1.05 350 *Airfoil sub-grid* mesh.

- the number of grid points on airfoil surface (from *Model 1*- 175 006 1.050 to *Model 1*-190 010 1.050);
- the distribution of grid points on airfoil surface, in particular, grid points were clustered close to the transition onset (from *Model 1'*- 140 006 1.050 to *Model 1'*- 400 010 1.050). These meshes were named as *Model 1'*.

3.5. *Model 2* airfoil sub-grid

In order to better capturing the flow features in the wake of the airfoil, a horizontal fully structured grid was created in the region behind the airfoil itself, thus obtaining a hybrid structured-triangular mesh, which was named *Model 2.* A high-quality structured mesh was created close to the airfoil surface in order to better resolve the boundary layer, while outside the boundary layer region a triangular unstructured grid was created using proper size functions.

In Figure 13 the main boundary conditions of *Model 2 Airfoil sub-grid* domain are shown, while in Figure 14 (a) a view of the global mesh is depicted and Figures 14 (b), (c) show some details of the grid boundary layer around the airfoil close to the leading edge and the trailing edge and wake regions respectively.

3.6. *Model 3* airfoil sub-grid

Conceived as a variant of *Model 2* mesh, a diverging fully structured grid was created in the region behind the airfoil itself, thus obtaining a hybrid structured-triangular mesh, which was named *Model 3.* In Figure 15 (a) a view of the global mesh is depicted, while Figures 15 (b), (c)
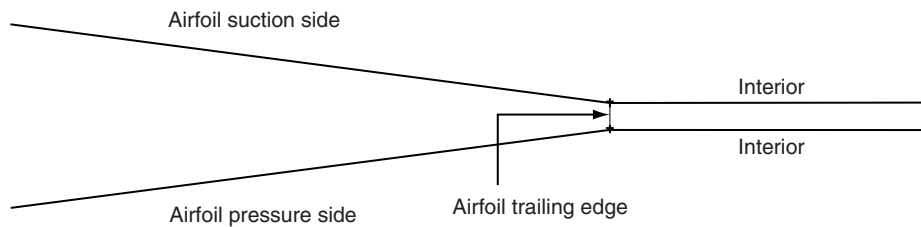

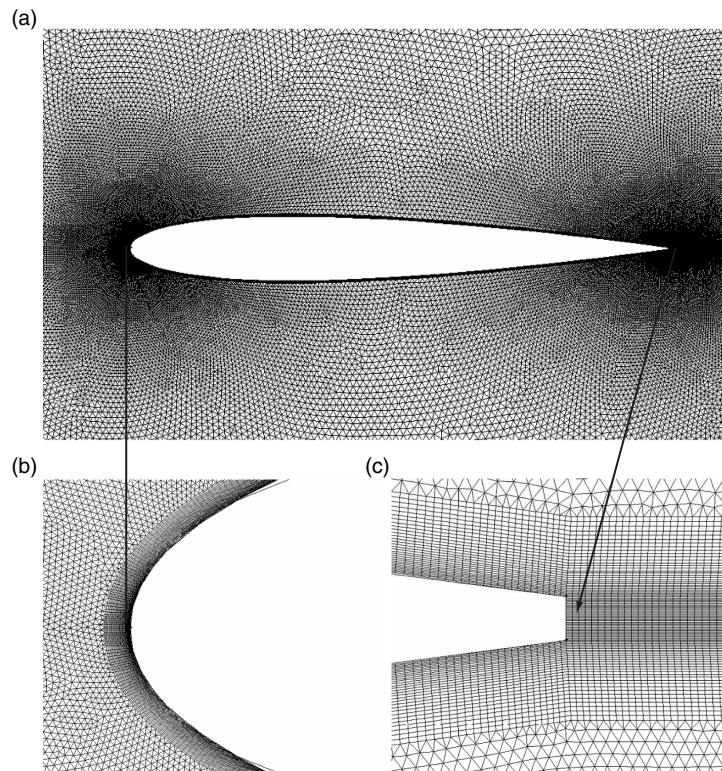Figure 13: Main boundary conditions of the *Wind Tunnel sub-grid* area for *Model 2.*

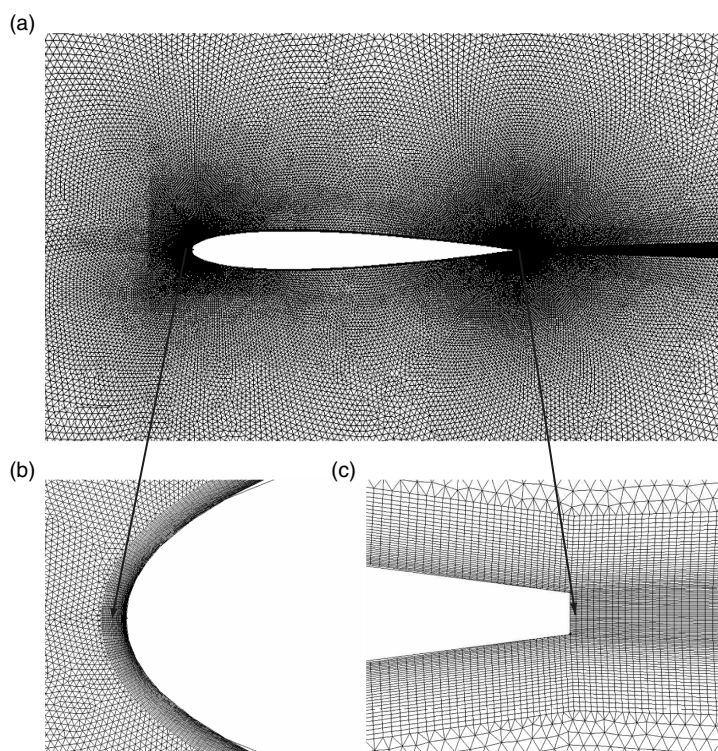Figure 14: *Model 2* – 350 37 400 *Airfoil sub-grid* mesh.

Figure 15: *Model 3 − 350 37 400 Airfoil sub-grid* mesh.

show some details of the grid boundary layer around the airfoil close to the leading edge and the trailing edge and wake regions respectively.

The characteristic data of grid boundary layers are the same as *Model 2* - 350 37 400.

4. SIMULATED FLOW CONDITIONS

Simulations were performed using the commercial RANS solver ANSYS FLUENT®, which implements 2-D Reynolds-averaged Navier-Stokes equations using a finite volume-finite element based solver. A segregated solver, implicit formulation, was chosen for unsteady flow computation.

The fluid was assumed to be incompressible, being the maximum fluid velocity on the order of 90 m/s. In order to obtain the desired blade Reynolds number of 360,000, the velocity inlet value was set to 61.3 m/s, being the chord length of 0.0858 m. A no-slip boundary condition was adopted for the airfoils walls.

In order to investigate the sensitivity of γ–θ transitional model to grid resolution, all mesh models were initially tested at 0 deg angle of attack and for a percent free-stream turbulence intensity of 1.33, which represents the code default value.

As a global convergence criterion, residuals were set to 10^{-5}. The simulations, performed on a 4 processor, 2.33 GHz clock frequency computer, required a total CPU time of about 1/2 hour each.

5. RESULTS AND DISCUSSION

Table 3 represents the CFD computed value of airfoil C_D for all the adopted grids.

The following observations can be drawn:

- the γ–θ transitional model is able to predict the laminar to turbulent transition, provided the mesh setup of the wall boundary layer is performed in order to ensure

Table 3: CFD computed value of airfoil C_D for all the adopted grids

Mesh name	C_D [–]	Mesh name	C_D [–]
Model 1 - 350 006 1.025	0.00844	*Model 0* - 1.05	0.00986
Model 1 - 350 006 1.050	0.00856	*Model 0* - 1.10	0.00933
Model 1 - 350 006 1.100	0.00852	*Model 1'* - 140 006 1.050	0.00845
Model 1 - 350 006 1.200	0.00859	*Model 1'* - 140 008 1.050	0.00846
Model 1 - 350 006 1.500	0.00919	*Model 1'* - 140 010 1.050	0.00848
Model 1 - 350 008 1.025	0.00849	*Model 1'* - 300 006 1.050	0.00849
Model 1 - 350 008 1.050	0.00856	*Model 1'* - 300 008 1.050	0.00842
Model 1 - 350 008 1.100	0.00869	*Model 1'* - 300 010 1.050	0.00850
Model 1 - 350 008 1.200	0.00855	*Model 1'* - 400 006 1.050	0.00856
Model 1 - 350 008 1.500	0.00947	*Model 1'* - 400 008 1.050	0.00854
Model 1 - 350 010 1.025	0.00851	*Model 1'* - 400 010 1.050	0.00855
Model 1 - 350 010 1.050	0.00859	*Model 2* - 175 8 332	0.00886
Model 1 - 350 010 1.100	0.00858	*Model 2* - 175 8 664	0.00887
Model 1 - 350 010 1.200	0.00858	*Model 2* - 175 8 1328	0.00885
Model 1 - 350 010 1.500	0.00909	*Model 2* - 350 8 664	0.00832
Model 1 - 175 006 1.050	0.00851	*Model 2* - 350 8 1328	0.00842
Model 1 - 190 006 1.050	0.00836	*Model 2* - 700 8 664	0.00857
Model 1 - 175 008 1.050	0.00841	*Model 2* - 700 8 1328	0.00857
Model 1 - 190 008 1.050	0.00835	*Model 2* - 350 37 400	0.00832
Model 1 - 175 010 1.050	0.00826	*Model 3* - 350 37 400	0.00846
Model 1 - 190 010 1.050	0.00836		

both a value of y^+ close to 1 and a number of no less than 10 boundary layer rows within the physical boundary layer;

·   all the adopted hybrid grids have y^+ values close to 1, as can be seen in Figure 16, but some of them (*Model 1* - 350 006 1.500, *Model 1* - 350 008 1.500, *Model 1* - 350 010 1.500) have a too small number of boundary layer rows within the physical boundary layer because of a too high value of the BL growth factor from airfoil surface to external computational domain. For these cases, the γ–θ transitional model is not able to
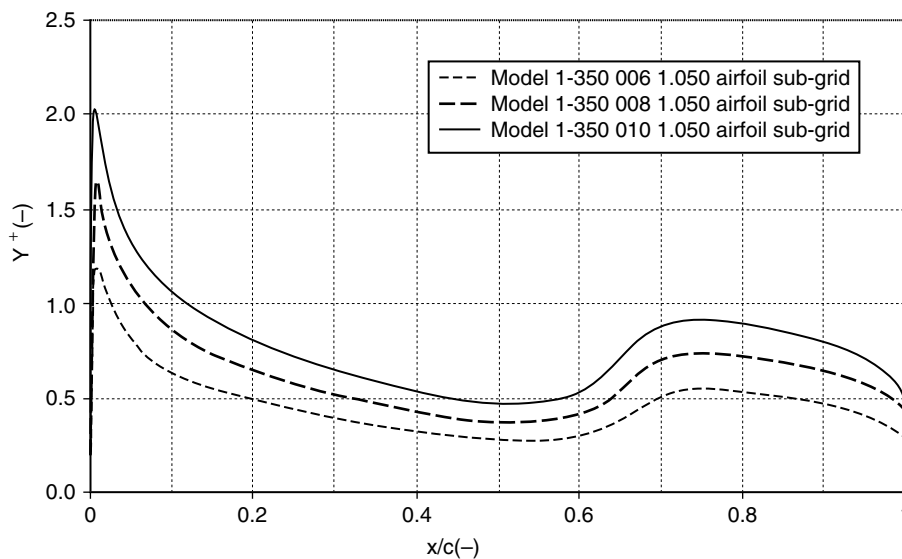

Figure 16: Comparison between y^+ distribution for *Model 1* - 350 006 1.050, *Model 1* - 350 008 1.050 and *Model 1* - 350 010 1.050 *Airfoil sub-grids*; A.O.A. = 0 deg.

correctly predict the laminar to turbulent transition and the calculated value of C_D is 7–8 % higher with respect to more refined grids;

· also triangular grids, though adopting a very high number of grid points on airfoil upper and lower surface (of the order of 10 times with respect to *Model 1* grids), are not able to predict the laminar to turbulent transition because of a too high value of the mesh growth factor from airfoil surface to external computational domain. Also for this case, the calculated value of C_D is 7–8 % higher with respect to hybrid refined grids;

· the clustering of grid points close to the transition onset shows little influence on the capabilities of the model to determine airfoil drag (the difference between *Model 1* and *Model 1'* computed C_D is close to 1 %);

· the use of a horizontal/diverging fully structured grid in the region behind the airfoil shows little influence on the capabilities of the model to determine airfoil drag (the difference between *Model 1*, *Model 2* and *Model 3* computed C_D is between 2 and 3 %).

On the basis of the above mentioned arguments, *Model 1- 350 006 1.050 Airfoil sub-grid* was chosen as the best compromise between grid prediction capabilities and total CPU time required in order to obtain convergence, as can be seen from Figure 17, showing a comparison between the computed drag coefficient for meshes from *Model 1- 350 006 1.025* to *Model 1- 350 006 1.500*.

Model 1- 350 006 1.050 Airfoil sub-grid was consequently used:

1. to explore the effect of freestream turbulence intensity on the transition onset and consequent airfoil skin friction coefficient distribution;
2. to explore also the range of airfoil angles of attack between 2 deg and 10 deg;
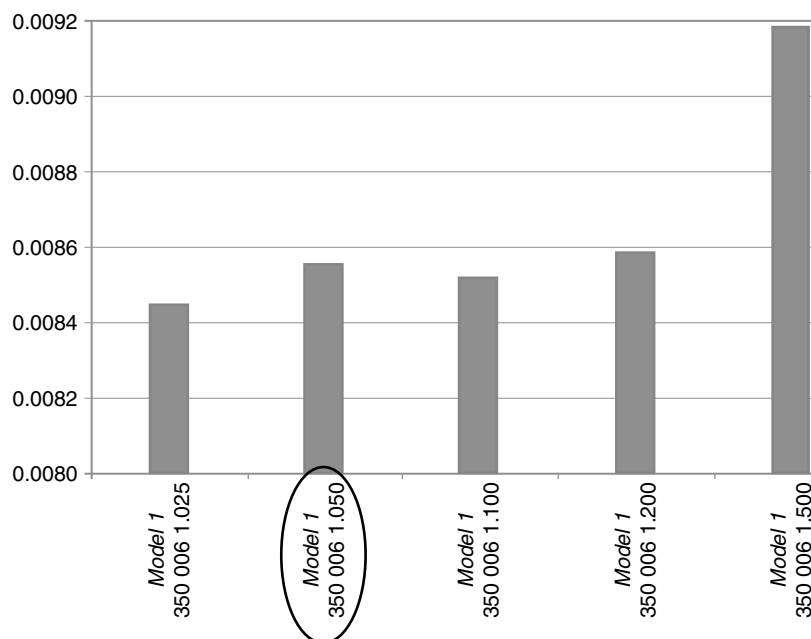3. to compare CFD predictions with experimental data and to XFOIL calculations.

Figure 17: Comparison between the computed drag coefficient for meshes from *Model 1 - 350 006 1.025* to *Model 1 - 350 006 1.500*. The circle evidences the selected grid.

Table 4: CFD calculated values of total drag coefficient, total skin friction coefficient, total drag coefficient and suction side transition point for *Model I* - 350 006 1.050 *Airfoil sub-grid*

FSTI [%]	K [m²/s²]	C_D [−]	$C_{D,skin}$ [−]	$C_{D,pressure}$ [−]	Suction side transition point [%]
1.0000	0.563654	0.007647	0.005213	0.002435	74
1.1250	0.713374	0.007799	0.005425	0.002373	71
1.1875	0.794840	0.007914	0.005590	0.002325	68
1.2500	0.880709	0.008099	0.005730	0.002370	66
1.3300	1.000000	0.008620	0.006245	0.002375	60
1.5000	1.268220	0.008868	0.006490	0.002378	54

Table 4 represents the CFD calculated values of total drag coefficient for *Model 1* − 350 006 1.050 *Airfoil sub-grid* as a function of the percent free-stream turbulence intensity parameter, showing also the values of airfoil total skin friction and pressure drag coefficients, defined as:

$$C_{D,skin} = \frac{D_{skin}}{\frac{1}{2}\rho c V_\infty^2} \tag{8}$$

$$C_{D,pressure} = \frac{D_{pressure}}{\frac{1}{2}\rho c V_\infty^2} \tag{9}$$

As suggested by Langtry and Menter [27], the onset of transition was judged as the location were the skin friction first started to increase due to the production of turbulent kinetic energy in the boundary layer.

As already noticed by Benini and Ponza [23], the effect of free-stream turbulence intensity on computed airfoil total drag is dramatically relevant: the increment of the FSTI value determines an anticipation of the laminar to turbulent transition onset and a consequent increase in calculated skin friction drag, as can be seen also in Figures from 18 to 20.

In order to gain the same total drag coefficient of experimental measurements for 0 deg A.O.A., CFD calculations were performed adopting a FSTI of 1.1875%. This value was also adopted in all subsequent CFD calculations for different values of angle of attack.

As can be drawn by the comparison between Tables 3 and 4, the sensitivity of the CFD code to free-stream turbulence intensity is much higher than to the wall y^+ parameter.

Tables 5 and 6 represent the CFD computed values of C_D and C_L for *Model 1* - 350 006 1.050 *Airfoil sub-grid* as a function of airfoil angle of attack, comparing CFD predictions to experimental data and also to XFOIL calculations. The latter were controlled by the N_{crit} parameter, which is the log of the amplification factor of the most-amplified frequency which triggers transition. A suitable value of this parameter depends on the ambient disturbance level in which the airfoil operates, and mimics the effect of such disturbances on transition. In order to gain the same total drag coefficient of experimental measurements for 0 deg A.O.A., XFOIL calculations were performed adopting a N_{crit} of 4.4000. This value was also adopted in all subsequent calculations for different values of angle of attack.

As can be clearly seen also from Figures 21 and 22, for angles of attack ranging from 0 deg to 4 deg, γ–θ transitional model drag prediction capabilities are very similar to XFOIL code
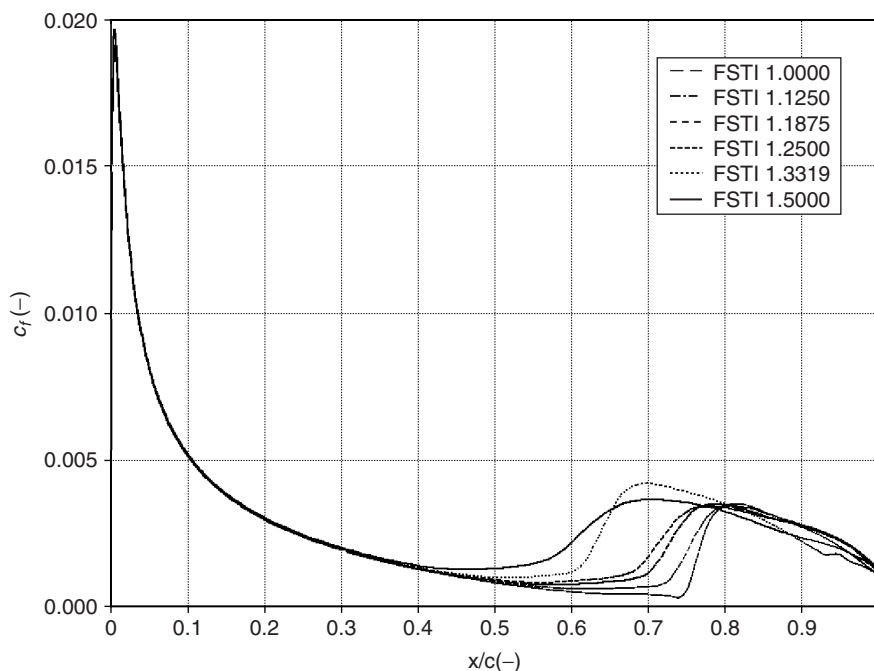
Figure 18: Anticipation of the laminar to turbulent transition onset as a function of the increment of the FSTI value; *Model 1 -* 350 006 1.050 *Airfoil sub-grid*, A.O.A. = 0 deg.
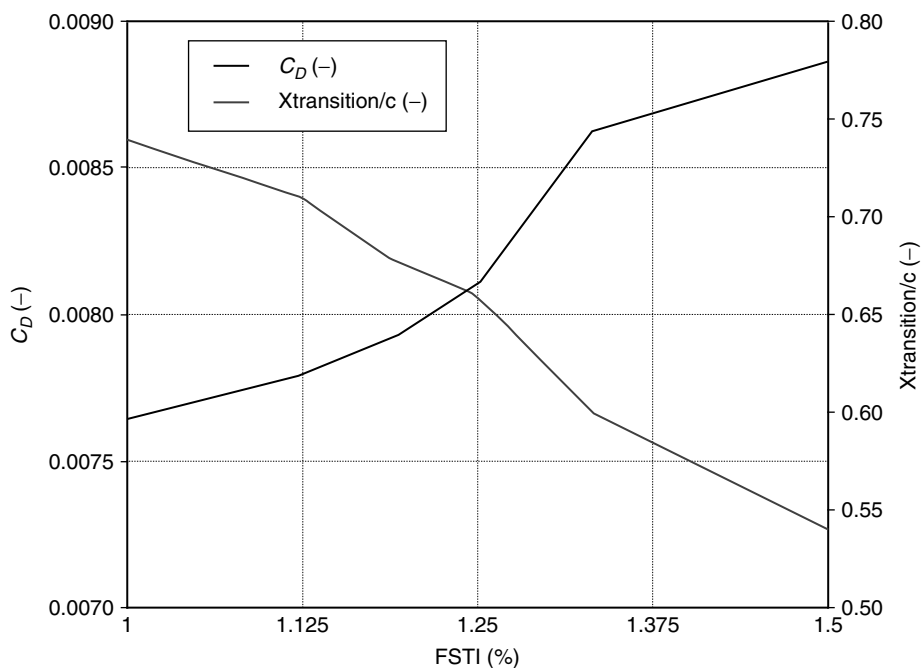

Figure 19: Correlation between total airfoil drag and laminar to turbulent transition onset as a function of the FSTI value; *Model 1 -* 350 006 1.050 *Airfoil sub-grid*, A.O.A. = 0 deg.

ones, while XFOIL still remains the best option for drag prediction at higher angles of attack, due to drag overestimation by the γ–θ transitional model. For angles of attack close to stall (10 deg) both codes show some limits in drag prediction capability.

On the other hand, γ–θ transitional model proves to be the best option for airfoil lift coefficient prediction, even for angles of attack close to stall, where XFOIL shows some limits.
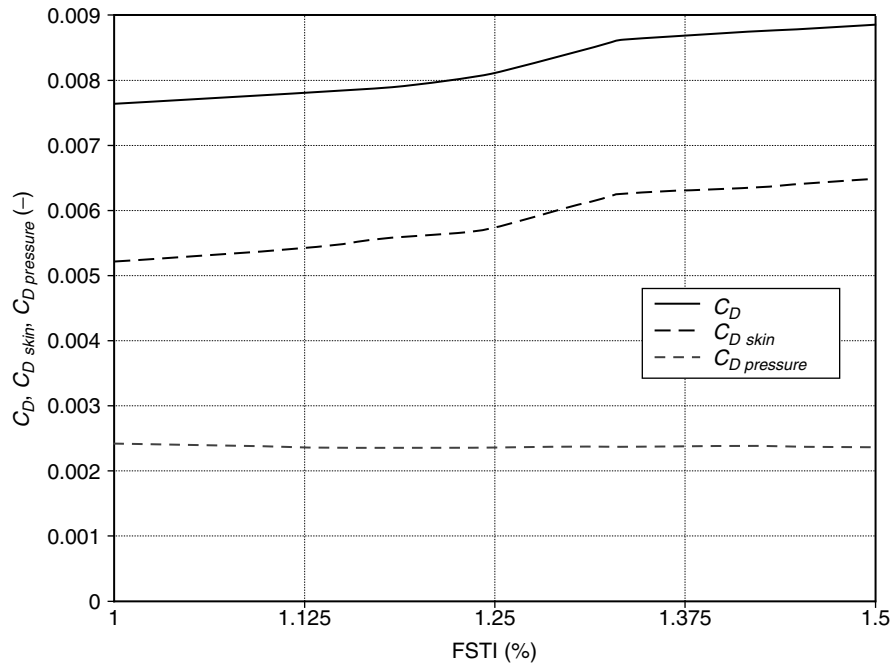
Figure 20: Increase in skin friction drag as a function of the increment of the FSTI value;
Model 1 - 350 006 1.050 *Airfoil sub-grid*, A.O.A. = 0 deg.

Table 5: Comparison between experimental, CFD and XFOIL airfoil total drag coefficients for angles of attack ranging from 0 deg to 10 deg; *Model 1 - 350 006 1.050 Airfoil sub-grid*

A.O.A. [deg]	C_D [–] (Sandia)	C_D [–] (CFD)	$(C_{D-CFD} - C_{D-Sandia})/ C_{D-Sandia}$ [%]	C_D [–] (XFOIL)	$(C_{D-XFOIL} - C_{D-Sandia})/ C_{D-Sandia}$ [%]
0	0.0079	0.0079	0.0	0.0079	0.0
2	0.0084	0.0083	−1.2	0.0084	0.0
4	0.0098	0.0094	−4.1	0.0102	4.1
6	0.0125	0.0134	7.2	0.0129	3.2
8	0.0153	0.0161	5.2	0.0158	3.3
10	0.0184	0.0213	15.8	0.0198	7.6

Table 6: Comparison between experimental, CFD and XFOIL airfoil total lift coefficients for angles of attack ranging from 0 deg to 10 deg; *Model 1 - 350 006 1.050 Airfoil sub-grid*

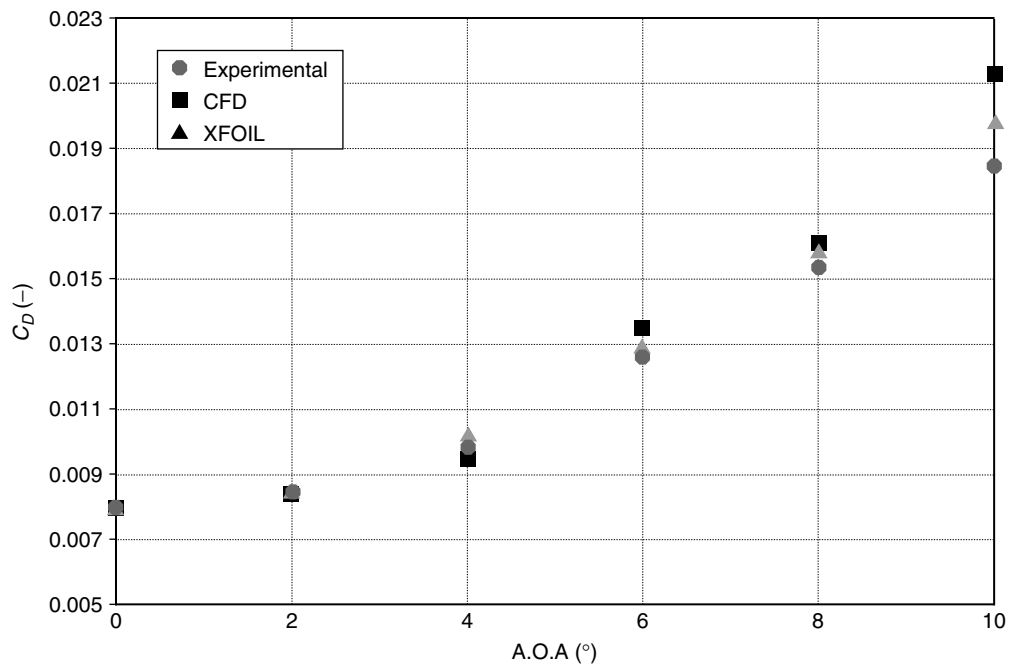| A.O.A. [deg]	C_L [–] (Sandia)	C_L [–] (CFD)	$(C_{L-CFD} - C_{L-Sandia})/ C_{L-Sandia}$ [-]	C_L [–] (XFOIL)	$(C_{L-XFOIL} - C_{L-Sandia})/ C_{L-Sandia}$ [%]
0	0.00	0.00	0.0%	0.00	0.0
2	0.22	0.22	0.0%	0.21	−4.5
4	0.44	0.42	−4.5%	0.43	−2.3
6	0.66	0.61	−7.6%	0.69	4.5%
8	0.85	0.82	−3.5%	0.88	3.5%
10	0.98	0.99	1.0%	1.04	6.1%

Figure 21: Comparison between experimental, CFD and XFOIL airfoil total drag coefficients for angles of attack ranging from 0 deg to 10 deg; *Model 1* - 350 006 1.050 *Airfoil sub-grid.*

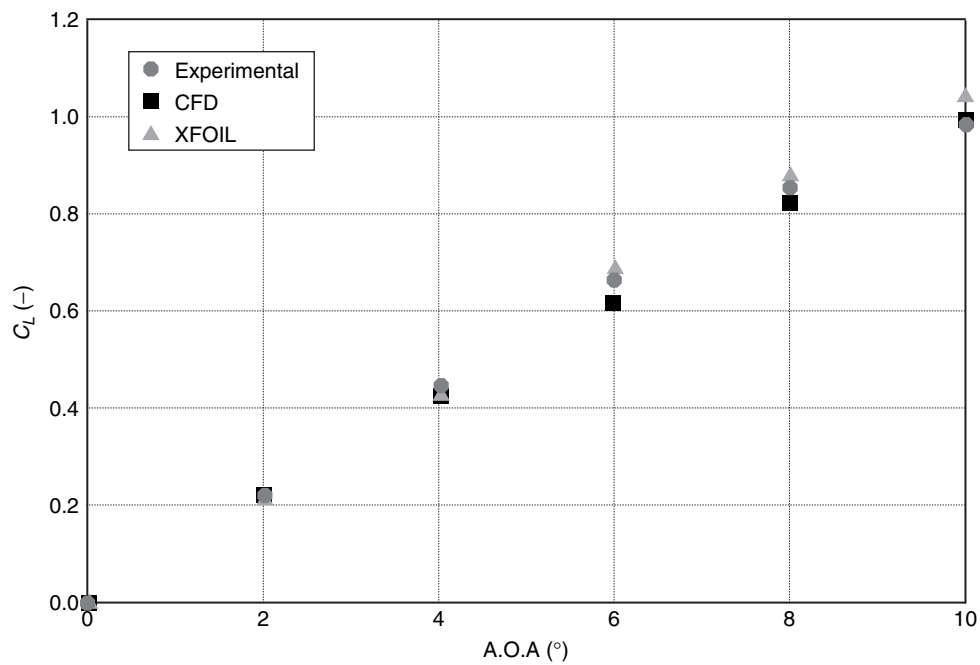
Figure 22: Comparison between experimental, CFD and XFOIL airfoil total lift coefficients for angles of attack ranging from 0 deg to 10 deg; *Model 1* - 350 006 1.050 *Airfoil sub-grid.*

Table 7: Comparison between CFD and XFOIL computed values of total skin friction drag, total pressure drag, total drag and suction side transition point for angles of attack ranging from 0 deg to 10 deg; *Model 1 - 350 006 1.050 Airfoil sub-grid*; (*) transition onset not clearly visible

A.O.A. [deg]	$C_{D,skin}/$ C_D [–] (CFD)	$C_{D,skin}/$ C_D [–] (XFOIL)	$C_{D,pressure}/$ C_D [–] (CFD)	$C_{D,pressure}/$ C_D [–] (XFOIL)	$x_{trans}/$ c [%] (CFD)	$x_{trans}/$ c [%] (XFOIL)
0	0.71	0.77	0.29	0.23	68	66
2	0.67	0.74	0.31	0.26	53	45
4	0.59	0.67	0.40	0.33	35	23
6	0.41	0.57	0.59	0.43	14	8
8	0.32	0.47	0.69	0.53	3(*)	4
10	0.23	0.36	0.76	0.64	2(*)	3

Table 7 represents a comparison between CFD and XFOIL computed values of total skin friction drag, total pressure drag and total drag for angles of attack ranging from 0 deg to 10 deg. Curiously, it can be noticed that CFD overestimation in airfoil total drag with respect to XFOIL predictions is due to overestimation of pressure drag, while skin friction drag results underestimated. The cause of this phenomenon is not yet clear and further research is to be done.

Contrary to the findings of Menter et al. [22] γ–θ model seems to predict the transition onset slightly downstream with respect to XFOIL, at least for lower angles of attack. Further research is to be done in order to better investigate the capability of the γ–θ transitional model to predict the location of the transition onset.

Figure 23 outlines the complete set of airfoil skin friction coefficient distributions for angles of attack ranging from 0 deg to 10 deg. A good agreement between CFD and XFOIL predictions can be noticed for airfoil pressure side, even up to 10 deg angles of attack, while for airfoil suction side agreement can be seen just up to 2 deg angles of attack, being very poor for higher values of angle of attack.

It can be noticed that, at higher angles of attack, the CFD skin friction distributions are jagged upstream of the transition point. This phenomenon suggests some numerical issue to be probably connected to the accuracy of the γ–θ transitional model for higher angles of attack, as already observed by Benini and Ponza [23]. Further investigation is required.
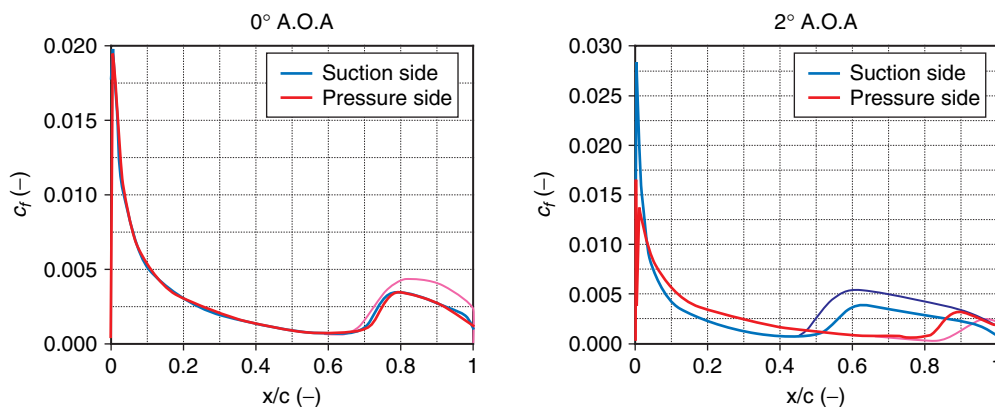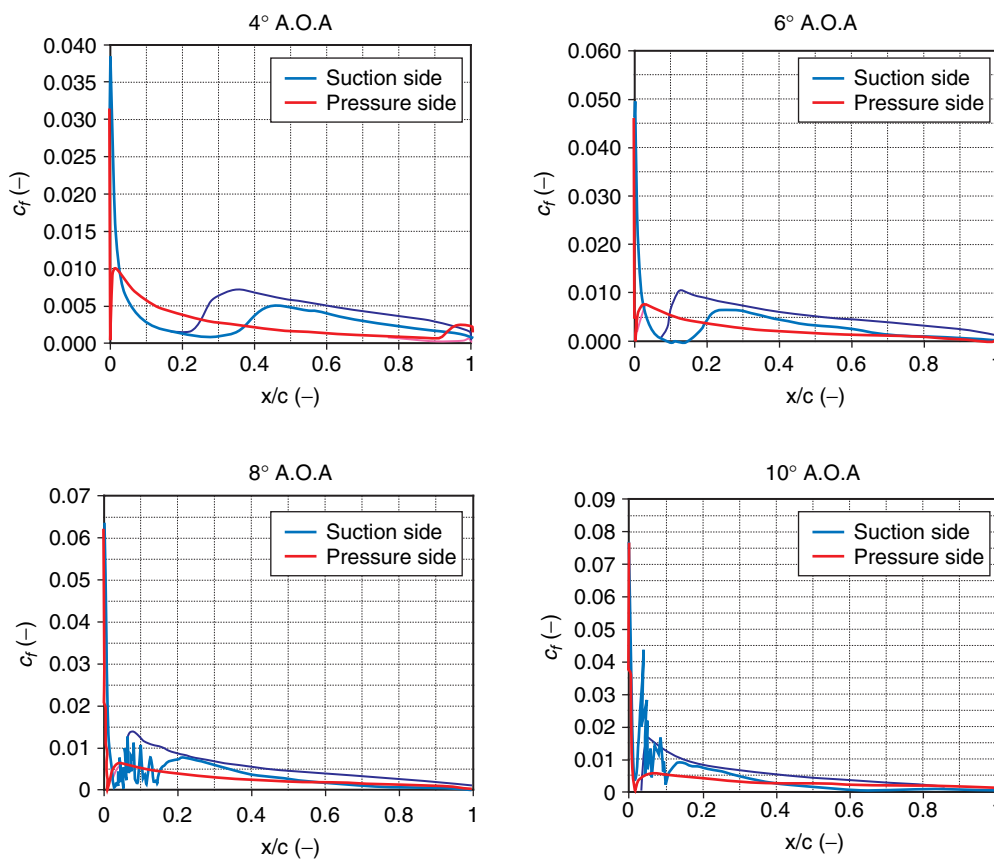

Figure 23: (*Continued*)

Figure 23: Comparison between skin friction coefficient distributions over the airfoil for angles of attack ranging from 0 deg to 10 deg; marked colour: CFD, weak colour: XFOIL.

6. CONCLUSIONS AND FUTURE WORKS

At a low airfoil Reynolds number, γ–θ transitional model was proved to be able to predict laminar to turbulent transition. Results were rather accurate for airfoil total lift coefficient (even better than XFOIL for high values of angle of attack), while airfoil total drag coefficient prediction capability was good for low values of angle of attack. As airfoil angle of attack increased, the discrepancies between CFD and XFOIL computed drag become higher, being XFOIL predictions closer to experimental data, due to drag overestimation by the γ–θ transitional model. This phenomenon was find to be due to pressure drag overestimation more than to skin friction drag overestimation by γ–θ transitional model and needs further investigations.

Agreement between CFD and XFOIL skin friction coefficient prediction was pretty good for airfoil pressure side at all angles of attack, while for airfoil suction side the agreement was acceptable only up to 2 deg angle of attack. Contrary to the findings of Menter et al. [9] γ–θ model seems to predict the suction side transition onset slightly downstream with respect to XFOIL, at least for lower angles of attack. Further research is to be done in order to better investigate the capability of the γ–θ transitional model to predict the location of the transition onset.

An accurate mesh setup of airfoil wall boundary layer proved to be necessary in order to correctly predict the laminar to turbulent transition: a too high value of the BL growth factor from airfoil surface to external computational domain resulted in an inability to predict the

transition onset because of a too small number of boundary layer rows within the physical boundary layer. Anyway, once the necessary grid refinement had been reached, the clustering of grid points close to the transition onset or the use of a horizontal/diverging fully structured grid in the region behind the airfoil was proved to have small influence on the code ability to predict the transition.

The numerical results need however to be interpreted since the experimental data are affected by the uncertainty on the turbulence intensity level. In order to overcome this source of uncertainty, different values of percent free-stream turbulence intensity were investigated, proving the sensitivity of the CFD code to free-stream turbulence intensity to be much higher than to the wall y^+ parameter.

REFERENCES

[1] Cahay, M., Luquiau, E., Smadja, C., Silvert, F., *Use of a Vertical Wind Turbine in an Offshore Floating Wind Farm*, Offshore Technology Conference, 2–5 May 2011, Houston, Texas, USA.

[2] Ljungstrom, O., *New concepts in vertical axis wind turbines /VAWT/ and applications to large multi-MW size, off-shore wind turbine systems*, Wind Energy Conference, Boulder, Colo., April 9–11, 1980, Technical Papers.

[3] Paulsen, U. S., Pedersen, T. F., Madsen, H. A., Enevoldsen, K., Nielsen, P. H., Hattel, J., Zanne, L., Battisti, L., Brighenti, A., Lacaze, M., Lim, V., Heinen, J. W., Berthelsen, P. A., Carstensen, P., de Ridder, E., van Bussel, G., Tescione, G., *Deepwind – An Innovative Wind Turbine Concept for Offshore*, EWEA 2011, 14–17 March 2011, Brussels, Belgium.

[4] Stannard, N., Bumby, J.R., *Performance aspects of mains connected small-scale wind turbines*, Generation, Transmission & Distribution, IET, Volume 1, Issue 2, March 2007, pp. 348–356.

[5] Chawla, J. S., *Low Reynolds Number Flow over Airfoils*, Mechanical Engineering Department, Indian Institute of Technology – Bombay, Seminar Report, Dec. 2009.

[6] Koch, L. D., *Design and Performance Calculations of a Propeller for Very High Altitude Flight*, Lewis Research Center, Cleveland, Ohio, February 1998, NASA/TM-1998-206637.

[7] Mueller, T. J., *Low Reynolds Number Vehicles*, Neuilly-Sur-Seine, France: Advisory Group for Aerospace Research and Development, NTIS, AGARDograph No. 288, 1985.

[8] Raciti Castelli, M., Pavesi, G., Battisti, L., Benini, E., Ardizzon, G.,: *Modeling Strategy and Numerical Validation for a Darrieus Vertical Axis Micro-Wind Turbine*, ASME 2010 International Mechanical Engineering Congress & Exposition, November 12–18, 2010, Vancouver, British Columbia, Canada, IMECE2010-39548.

[9] Templin, R. J.: *Aerodynamic Performance of Vertical-Axis Wind Machines*, ASME Paper 75-WA/ENER-1, 1975.

[10] Strickland, J. H.: *The Darrieus Turbine: A Performance Prediction Model Using Multiple Streamtube*, SAND75-0431.

[11] Gregory, N., O'Reilly, C. L., *Low-Speed Aerodynamic Characteristics of NACA 0012 Aerofoil Section, including the Effects of Upper-Surface Roughness Simulating Hoar Frost*, Aeronautical Research Council, Reports and Memoranda No. 3726, January 1970, Printed in England for Her Majesty's Stationery Office by J. W. Arrowsmith Ltd, Bristol BS3 2NT – Dd. 505715 K5 10/73.

[12]   Sheldahl, R. E., Klimas, P. C., *Aerodynamic Characteristics of Seven Symmetrical Airfoil Sections Through 180-Degree Angle of Attack for Use in Aerodynamic Analysis of Vertical Axis Wind Turbines*, SAND80-2114, Unlimited Release, UC-60.

[13]   Drela, M., *An Analysis and Design System for Low Reynolds Number Airfoils*, Conference on Low Reynolds Number Airfoil Aerodynamics, University of Notre Dame, June 1989.

[14]   Drela, M., Giles, M. B., *Viscous-Inviscid Analysis of Transonic and Low Reynolds Number Airfoils*, AIAA Journal, 25(10), pp. 1347–1355, October 1987.

[15]   Drela, M., Integral Boundary Layer Formulation for Blunt Trailing Edges, Paper AIAA-89-2166, August 1989.

[16]   Raciti Castelli, M., *Analisi numerica delle prestazioni di una micro-turbina eolica ad asse verticale modello Darrieus*, PhD Thesis, Università di Padova, Italy, 2010.

[17]   Raciti Castelli, M., Englaro, A., Benini, E., *The Darrieus Wind Turbine: Proposal for a New Performance Prediction Model Based on CFD*, Energy 36 (2011), pp. 4919–4934.

[18]   Johansen J., *Prediction of Laminar/Turbulent Transition in Airfoil Flows*, Risø National Laboratory, Roskilde, Denmark, May 1997, Risø-R-987(EN).

[19]   Lombardi, G., Salvetti, M. V., Pinelli, D., *Numerical Evaluation of Airfoil Friction Drag*, J. Aircraft, Vol. 37, No. 2, pp. 354–356, 2000.

[20]   Lian, Y., Shai, W., *Laminar-Turbulent Transition of a Low Reynolds Number Rigid or Flexible Airfoil*, AIAA Journal, Vol. 45, No. 7, July 2007, pp. 1501–1513.

[21]   Menter, F. R., Langrty, R. B., Likki, S. R., Suzen, Y. B., Huang, P. G., Völker, S., *A Correlation-Based Transition Model Using Local Variables – Part I: Model Formulation*, Journal of Turbomachinery, Volume 128, Issue 3, pp. 413–422, 2006.

[22]   Menter, F. R., Langrty, R. B., Likki, S. R., Suzen, Y. B., Huang, P. G., Völker, S., *A Correlation-Based Transition Model Using Local Variables – Part II: Test Cases and Industrial Applications*, Journal of Turbomachinery, Volume 128, Issue 3, pp. 423–434, 2006.

[23]   Benini, E., Ponza, R., *Laminar to Turbulent Boundary Layer Transition Investigation on a Supercritical Airfoil Using the γ–θ Transitional Model*, 40th Fluid Dynamics Conference and Exhibit, 28 June – 1 July 2010, Chicago, Illinois, AIAA 2010–4289.

[24]   Hosseinverdi, S., Boroomand, M., *Prediction of Laminar-Turbulent Transitional Flow over Single and Two-Element Airfoils*, 40th Fluid Dynamics Conference and Exhibit, 28 June – July 2010, Chicago, Illinois, AIAA 2010–4290.

[25]   Wang, S., Ma, L., Ingham, D. B., Pourkashanian, M., Tao, Z., *Turbulence Modelling of Deep Dynamic Stall at Low Reynolds Number*, Proceedings of the World Congress on Engineering 2010, Vol. II, ISBN: 978-988-18210-7-2, VCE 2010, June 30 – July 2, 2010, London, UK.

[26]   *Information for Users of the Walter H. Beech Memorial Low-Speed Wind Tunnel*, Wichita State University Aeronautical Engineering Department, July 1966.

[27]   Langtry, R. B., Menter, F. R., *Transition Modeling for General CFD Applications in Aeronautics*, AIAA 2005–522.